Materials Science & Engineering A 718 (2018) 350–362

Contents lists available at ScienceDirect

Materials Science & Engineering A

journal homepage: www.elsevier.com/locate/msea

The effects of Silicon and Copper on microstructures, tensile and Charpy properties of weld metals by refined X120 wire

R. Cao[a,*], Z.S. Chan[a], J.J. Yuan[a], C.Y. Han[a], Z.G. Xiao[b], X.B. Zhang[a], Y.J. Yan[a], J.H. Chen[a]

[a] State Key Laboratory of Advanced Processing and Recycling of Non-ferrous Metal, Department of Materials Science and Engineering, Lanzhou University of Technology, Lanzhou 730050, People's Republic of China

[b] Hobart Brothers Company, An ITW Welding Company, Troy, OH 45373, USA

ARTICLE INFO

Keywords:
Low-alloy high-strength X120 steel
Ductile-brittle transition temperature
Toughness
Microstructure
Cleavage fracture

ABSTRACT

This paper analyzes the micro-mechanism of decrease of impact toughness with increasing Silicon and increasing Copper in weld metal of a low-alloy high-strength X120 steel. By comparing the microstructures, measuring the extending length of the fibrous crack, and calculating the local cleavage fracture stress σ_f, and then using the basic principles of the micro-mechanism of cleavage fracture, the essential causes of change of toughness in the weld metal of high-strength steel welded joints are revealed in this work.

1. Introduction

Over recent years, explorers have discovered crude oil and natural gas reservoirs that have caused an increasing demand in many manufacturing industries; because of this new demand, development of high strength steel gas pipelines and corresponding welded materials and welding technology have become a vital asset to tomorrow's economy. The corresponded mechanical properties are summarized in Table 1 [1].

In Ref. [2], the authors systematically summarized the possible causes on pipeline failure; these results indicated that in welded structures, weld metal and heat affected zone (HAZ) are the most prone locations for failure.

However, in recent years, researchers and practitioner have continuously developed new technologies and materials in the field of pipe welding and pipeline fabrication so that they might increase the longevity of the pipeline welded structures. Series studies have been centralized around the development of better microstructure leading to enhanced properties in welded joints, mainly, are addition and optimization of alloying elements in the weld [3–11]; development of filler materials [12]. In order to further enhance the applicability of high strength low alloy (HSLA) pipeline steels, understanding about the effect of alloying on the behavior of welded joint has a significant role. Professor Jaberi, & Kokabi [4] revealed the influence of nickel and manganese on microstructure and mechanical properties of shielded metal arc-weld API-X80 steel. It was found that Ni and Mn elements change the microstructure and mechanical properties in the as-deposited zone and reheated zone. With the increase of Ni and Mn contents, the proportion of acicular ferrite (AF), bainite and martensite-austenite (M-A) structure was increased. High Mn and Ni contents tend to promote micro-segregation of Mn, Ni, and Si in a network or parallel to grain boundaries in reheated zone. Professor Frantov et al [9] studied weldability of niobium-containing high-strength steel for pipelines. Results indicated that investigated steels with Nb content up to 0.1% do not have a tendency for cold cracking in the HAZ during welding, even with very low heat input. Professor Sirin et al [12] optimized the chemical compositions of weld electrodes to get the enhanced properties in the welded joint of X65 steel. Results indicated that to get higher impact toughness of the weld metal (WM) matched to that of base metal, increasing Mn content of the weld electrode is necessary. The existence of Ti in the weld electrode improves the impact toughness and ductility with a slight loss of tensile strength of WM with an increase of Ti content. Ref [13] discussed the effects of Si on the mechanical properties of a 0.4 carbon low alloy steel. Results indicated that additions of 2 wt pet Si make the yield strength increase from 1657 MPa to 1772 MPa, ultimate tensile strength increases from 1974 MPa to 2034 MPa, reduction in area increases from 38% to 41%. Si additions were also reported [14] to result in fewer and slightly larger eutectic carbides which was attributed to the possible inhibition of carbide nucleation by Si. In Ref [15], with the increasing of Cu content from 0% to 1.5%, the volume fraction of granular bainite (GB) decreased from 0.9 to 0.57, AF increased from 0.06 to 0.2, martensite (M) increased from 0.04 to 0.23, yield strength and tensile strength were increased, elongation were decreased, and ductile-brittle transition temperature (DBTT) was increased.

* Corresponding author.
E-mail address: caorui@lut.cn (R. Cao).

https://doi.org/10.1016/j.msea.2018.01.080
Received 24 December 2017; Received in revised form 16 January 2018; Accepted 21 January 2018
Available online 31 January 2018
0921-5093/

Table 1
Basic mechanical parameters of X80, X90, X100, X120 steels.

Steel grade	Yield Strength,Rt0.5 / MPa		Tensile strength, Rm / MPa	
	Min	Max	Min	Max
X80M	555	705	625	825
X90M	625	775	695	915
X100M	690	840	760	990
X120M	830	1050	915	1145

In order to further enhance the applicability of HSLA pipeline steels, understanding about the effect of alloying on the behavior of welded joint has a significant role. Based on above summaries, to obtain the satisfied weld metal with higher strength and higher toughness which matched to that of base metal, the study on chemical is still needed. Therefore, in this paper, the effects of element Si and element Cu on the microstructure, tensile and charpy properties of X120 pipeline steel will be further investigated. Firstly, the microstructure was systematically characterized by Optical Microscopy (OM), Scanning Electron Microscopy (SEM), Electron Backscattered Diffraction (EBSD), and Transmission Electron Microscopy (TEM), then tensile properties and Charpy toughness were measured at various testing temperatures. Next, the fracture surfaces of all testing specimens were observed and analyzed. Finally, FEM calculation has been used to calculate cleavage fracture stress to further compare and analyze the mechanisms of the effects of Si and Cu on Charpy toughness.

2. Experimental materials and procedures

2.1. Materials and welding procedures

A514 base plate with thickness of 18 mm was used as in this paper. The filler materials were metal power-cored wires with the diameter of 1.6 mm and various Si contents ranged 0.3%, 1.2% and 2.1%, and various Cu contents with 0.045% and 0.18%. The chemical compositions of the wires are listed in Table 2.

To avoid the dilution of the weld metal by the base metal, buttering welding was performed in 18 mm deep V-groove in the base steel plate before the deposition of the first-pass weld bead. The multi-pass bead was deposited using a gas metal arc welding process with a heat input of approximately 2.2KJ·mm^{-1}. The inter-pass temperature of 423K (150 °C)and the shielded gas of 80%Ar + 20%CO_2 were selected. Four weld metals with various Si and Cu contents were produced, the chemical compositions of the weld metals are listed in Table 3.

2.2. Microstructural analyses

After welding, metallographic specimens were cut from the weld joints using an electrical discharge cutting machine. Then, the specimens were ground, polished, and etched using a solution of 3 pct nitric acids in ethanol for observation. The microstructures of weld metals were observed by OM, SEM, and TEM.

Table 2
Chemical compositions of the wires (wt%) (+ /− 0.1%).

#	C	Si	Mn	Ni	Cr	Mo	Cu	Zr	P	S
1	0.06	0.3	1.4	2.0	0.22	0.25	0.045	0.014	0.006	0.003
2	0.06	1.2	1.4	2.0	0.22	0.25	0.045	0.014	0.006	0.003
3	0.06	2.0	1.4	2.0	0.22	0.25	0.045	0.014	0.006	0.003
4	0.06	0.3	1.4	2.0	0.22	0.25	0.180	0.014	0.006	0.003

Table 3
Chemical compositions of the weld metals (wt%).

#	C	Si	Mn	Ni	Cr	Mo	Cu	Zr	P	S
1	0.064	0.366	1.458	2.264	0.235	0.280	0.045	0.003	0.011	0.009
2	0.052	1.180	1.600	2.158	0.246	0.296	0.032	0.003	0.008	0.009
3	0.051	2.000	1.651	2.060	0.245	0.301	0.049	0.003	0.006	0.01
4	0.055	0.345	1.552	2.193	0.251	0.310	0.188	0.003	0.010	0.01

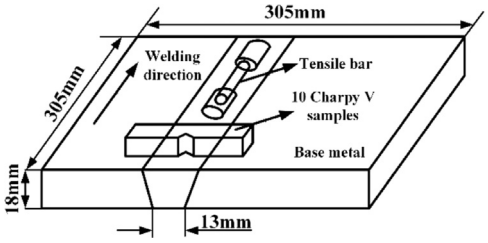

Fig. 1. Schematic and dimensions for sampling the tensile and Charpy V specimens.

2.3. EBSD analyses

To further clearly characterize the phase and misorientation, EBSD technique by an orientation imaging microscopy (OIM) was used in a JEOL6500 SEM which was operated at 20 kV. A 160 μm × 160 μm EBSD area scan was performed using a hexagonal grid with a step size of 0.28 μm.

2.4. Mechanical experiments

The tensile specimens and Charpy impact specimens were prepared from the welded joints. The sampling schematic is shown in Fig. 1. Tensile tests were carried out by the tester SHIMADZU AG-10T at RT, −50 °C, −80 °C, −110 °C, and −196°C respectively. Charpy V impact tests were carried out using a 450-J instrumented pendulum impact tester for specimens at RT, −50 °C, −80 °C, −110 °C, and −196 °C. Load-displacement curves and absorbed energy were measured by the instrumented Charpy V impact tester. A typical figure is presented in Fig. 2. Micro-hardness was measured by Micro-hardness Tester (HVT-1000A). For each measurement, a total of nine indents were made. The average Vickers hardness was determined.

The total absorbed energy was designated as the CVN energy. The dynamic yield strength σ_{yd} was calculated from the measured dynamic yield load Py by the following formula.

$$\sigma_{yd} = 2.99\ Py\ W/B(W-a)^2 \quad (1)$$

Where W is the height, B is the thickness, a is the notch depth of the Charpy specimen.

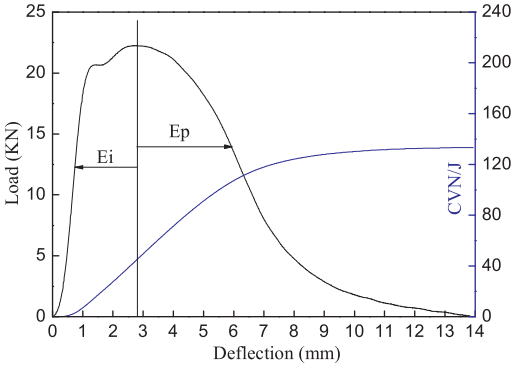

Fig. 2. A typical load-displacement and absorbed energy curves measured by the instrumented Charpy V impact tester.

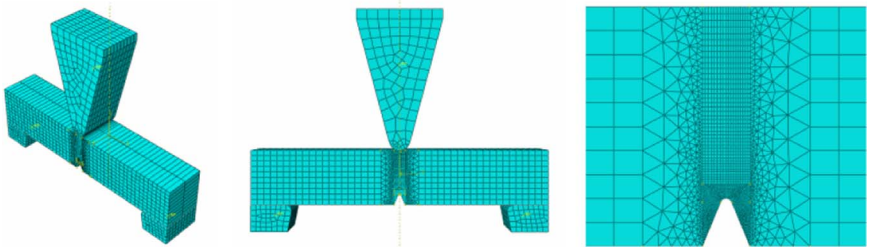

Fig. 3. FEM model and mesh distribution for a Charpy V specimen.

2.5. Observation and micro-parameter measurement on fracture surface

The fracture surfaces of broken tensile specimens and Charpy V specimens were observed in details by SEM Quanta 450 FEG (Field Emission Gun). The sites of crack initiation were identified by tracing back the river pattern strips on the fracture surface. The nature of the initiation particle was clarified by Energy Dispersive Spectrometer (EDS). The relative microscopic parameters including stretch zone width (SZW), fibrous crack length (SCL), and fracture distance X_f were measured for analyzing the micromechanism of fracture. The detailed study can be referred in chapter 3 of Ref. [16].

2.6. Finite element method (FEM) calculation

FEM calculation uses ABAQUS/Explicit code. Elements of 8-node linear brick, reduced integration, hourglass control (C3D8R) and 6-node linear triangular prism (C3D6) were taken to form the mesh of the body and the transition region separately. The number of the nodes are 9480, number of elements are 6912. Fig. 3 depicts the FEM model and mesh distribution for the Charpy V specimen. The measured power-exponent hardening classic flow curves have been input into the FEM model as material's properties.

3. Experimental results

3.1. The microstructures of the weld metals

To reveal the microstructure, the macro-feature of the multi-layer weld metal was presented in Fig. 4. From Fig. 4, two typical zones including the original weld metal and the reheated weld metal need to be analyzed. In the Fig. 5, two zones for each of four weld metals were presented. The component of microstructure in each weld are listed in Table 4. For weld metal 1 with 0.366% Si, the microstructure of the original weld metal mainly consists of coarse block ferrite (BF), granular bainite (GB) and lath bainite (LB). The microstructure of reheated weld metal is composed of fine uniform block ferrite (BF), acicular ferrite (AF), and granular bainite (GB). For weld metal 2 with 1.18% Si, the microstructure of the original weld metal is composed of BF, LB, and GB. However, amounts of fine uniform BF, AF, and minor GB dominated the microstructure of reheated weld metal. For weld metal 3 with 2.0% Si, the microstructure of the original weld metal is composed of GB, LB and amounts of martensite (M). The microstructure of reheated weld metal is composed of LB and amounts of GB. For weld metal 4 with 0.345% Si and 0.188% Cu, the microstructure of the original weld metal is different from the microstructures of above three original weld metals, some AF, coarse BF and minor GB are produced. The microstructure of reheated weld metal is composed of BF, AF and amounts of GB. The change of hardness for four weld metals is shown in Fig. 6. The hardness is changed from 248 to 302, 269–309, 295–382, 221–253, which is consistent with the microstructures as shown in Fig. 5.

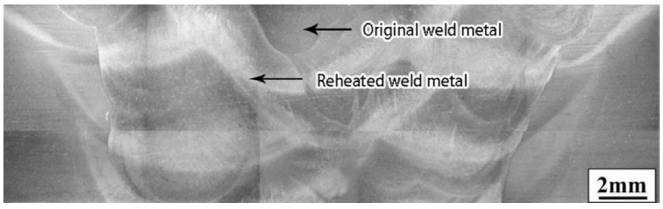

Fig. 4. Macro microstructure of the weld metal.

The histograms and distribution of grain sizes of four weld metals were shown in Table 5 and Fig. 7. The grain size of four original metals are 11–37 μm, 11–37 μm, 11–63 μm, 11–37 μm. The grain size of four reheated weld metals are 13–38 μm, 13–38 μm, 17–67 μm, 13–38 μm. And the prior austenite grain sizes were presented in Fig. 8. From Fig. 8, the prior austenite grain size of four weld metals are 23–74 μm, 21–87 μm, 31–108 μm, 33–83 μm, the prior austenite grain size of four reheated weld metals are 27–78 μm, 29–94 μm, 39–114 μm, 37–87 μm.

3.2. EBSD results of the weld metals

Fig. 9 shows histograms of low angle misorientation grain boundary (LAGB) , high angle misorientation grain boundary and Coincidence Cite Lattice (ΣCSL). It is seen that the fractions of high angle (>15°) misorientation grain boundaries (HAGB) of various weld metals do no show obvious change, however the ΣCSL of 2# weld metal is much higher than others.

3.3. TEM results of four weld metals

Fig. 10 shows the TEM results of four weld metals. BF, GB (Fig. 10(a)) and LB (Fig. 10(b)) with retained austenite compose the major microstructure in the weld metal 1#. Similar microstructural components are also observed in the weld metal 2#, but the uniform elongation of retained austenite is improved. For weld metal 3# with 2.0% Si, the weld metal is composed of LB, GB and M with high density dislocations. For weld metal 4 with 0.345% Si and 0.188% Cu, the microstructure of the weld metal is different from the microstructures of above three weld metals, AF, coarse BF and minor GB are produced.

3.4. The tensile properties of four weld metals

The average data of measured tensile ultimate strength, yield strength, and the reduction rate of fracture area in tensile tests at various temperatures were plotted in Fig. 11. From Fig. 11, with the decrease of the testing temperature, the ultimate tensile strength (σ_b), yield strength (σ_y) increase, and the fracture area reduction rate (ψ) decrease slightly. However, the degree of the decrease in these parameters is different. For example, there are slightly decrease for fracture area reduction rate for 1# specimen with 0.4 wt% Si, ie. decrease from 70.57% at 20 °C to 59.70% at −196 °C. For 2# specimen with 1.2 wt% Si, the reduction ratio of fracture area decreases from 60.84% at 20°C to 11.83% at −196 °C. At the same testing temperature, with the increase of Si content, σ_b, σ_y increase, ψ decreases; with the increase of Cu content, σ_b, σ_y and ψ decreases, which are related to the change of the microstructure in Fig. 5, the coarse grain size and coarse prior austenite grain size and the lower hardness in Fig. 6. Besides, the degree of decrease of fracture area reduction rate becomes larger in 3# specimen

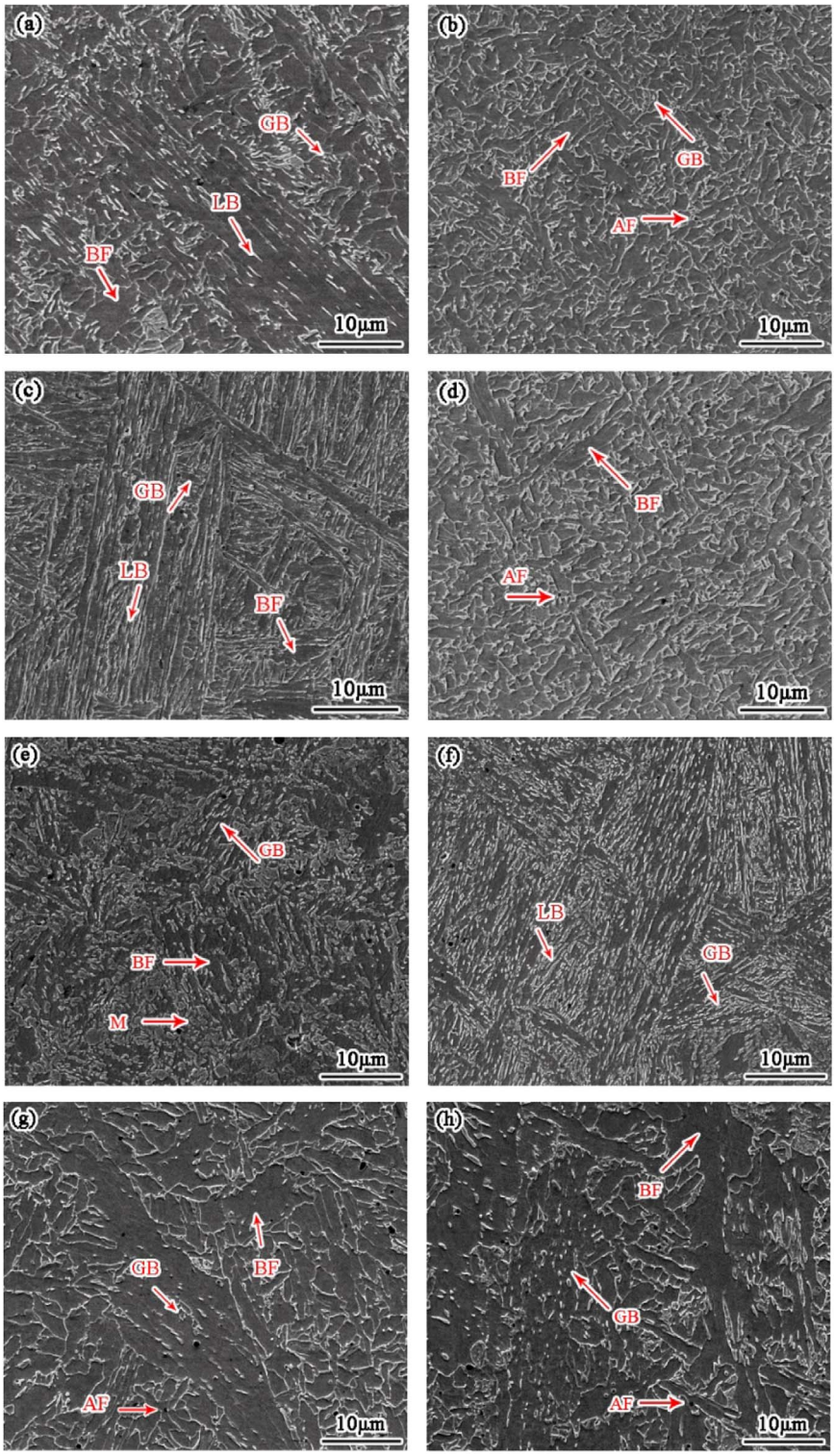

Fig. 5. Microstructures of four weld metals. (a) Original weld metal of 1#, (b) Reheated weld metal of 1#, (c) Original weld metal of 2#, (d) Reheated weld metal of 2#, (e) Original weld metal of 3#, (f) Reheated weld metal of 3#(g) Original weld metal of 4#, (h) Reheated weld metal of 4#.

Table 4
The component of microstructure in each weld.

#	Original weld metal	Reheated weld metal
1	55.4% BF + 19.6% GB + 25% LB	78.1% BF + 6.9% AF + 15% GB
2	1.8% BF + 84%GB + 14.2% LB	93.7% BF + 6.3% AF
3	11.4% BF + 13.3% GB + 75.3% M	2.8% BF + 85.3% GB + 11.9% LB
4	84% BF + 4.3% AF + 11.7 GB	47.3% BF + 15.9% AF + 36.8% GB

with 2.0% Si. And some unusual phenomenon are seen in 3# specimen with 2.0% Si at −50 ℃ and −196 ℃.

3.5. The fracture surface of tensile specimens

To reveal the difference of the tensile properties, the fracture surface was carefully observed. In this study, the fracture surface of 1# weld metal tensile specimen shows the typical fracture mode caused by the necking, as shown in Fig. 12.

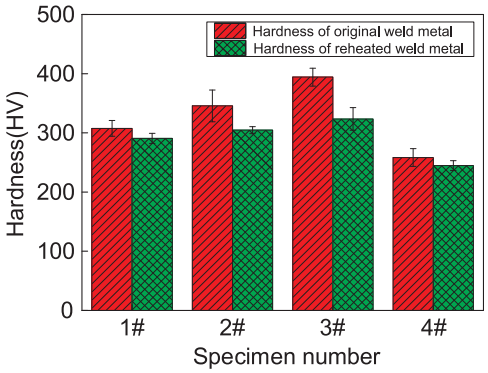

Fig. 6. Hardness of four weld metals.

Table 5
The histograms of grain sizes of four weld metals (μm).

#	Original weld metal	Reheated weld metal	Prior austenite of original weld metal	Prior austenite of original weld metal
1	11–37	11–38	23–74	27–78
2	11–27	11–38	21–87	29–94
3	11–36	17–67	31–108	39–114
4	11–37	11–38	33–83	37–87

Fig. 13 presents macro-fracture surfaces of four tensile specimens at various testing temperature. The morphologies of the fracture surfaces shown in Fig. 13(a) is the typical ones for high strength steel fractured at −50 ℃. The fracture surface is composed of three regions: center fibrous-initiation region (noted by arrow "FI"), middle shear-radical region (noted by arrow "SR") and outer shear-lip region (noted by arrow "SL"). The fracture surface of the specimen 3# is composed of two various regions A and B as shown in Fig. 13(c, d), yellow-brown A region is actually cracked before tensile fracture, dark gray B region with normal fracture color is fractured during tensile processes. The region A of 13(c) with above 80% quasi-cleavage fracture morphology dominated the fracture surface, which is fracture surface formed by a hydrogen induced crack. B region indicates the obvious microscopic cleavage surface with river pattern. In the A and B regions, four randomly selected points were analyzed by the EDS energy spectrum, the results are shown in Table 6. By comparison of the composition in A region and the B region, it was found that a high content of oxygen and Si enrichment in A region. In Fig. 14(a), there are two transverse cracks on the macro surface of 3# specimen at the temperature of −50 ℃, which indicates that the specimen is fractured at the transverse crack in the tensile test. For 3# specimen, un-regular fracture surfaces can be found. The fracture surface of 3# at −50 ℃ is showed in Fig. 14(b, c), it means that the lower tensile mechanical properties of specimen with 2.0 wt% Si is related to hydrogen induced cracking when the content of Si increases to 2%. Fig. 13(e) shows the fracture surface of specimen 4#, which is fully similar to that of the specimens 1#. By comparison of three regions, it was found that the fraction of plastic zone decreased.

3.6. The results of Charpy toughness

Fig. 15 presents the results between Charpy toughness and testing temperatures. The DBTT for four weld metals are −60 ℃, −41 ℃, −18 ℃, −56 ℃ respectively. The smaller the DBTT is, the better the toughness of the material is. DBTT increases with the increase of Si and Cu content. So, for the weld metals 1#, 2#, 3# with various Si contents, the weld metal 1 with 0.4 wt%Si has higher impact toughness. For weld metals 1#, and 4# with various Cu contents and the same Si content, the weld metal 1# with 0.045 wt% Cu has higher impact toughness.

3.7. The observed results of Charpy fracture surface

Fig. 16 shows Charpy V-type notch specimens fractured at RT (20 ℃). The ductile rupture with dimple pattern dominates the fracture of weld metals 1#, 2#, 4# at room temperature, as shown in Fig. 16 (a), (b), (d). However, for 3# weld metal, quasi-cleavage fracture modes have appeared even at room temperature as shown in Fig. 16(c). Thus, it is found that the fracture modes at room temperature are changed from dimple fracture to quasi-cleavage fracture with the increase of Si content from 0.366% to 2%. For weld metals with the same Si content

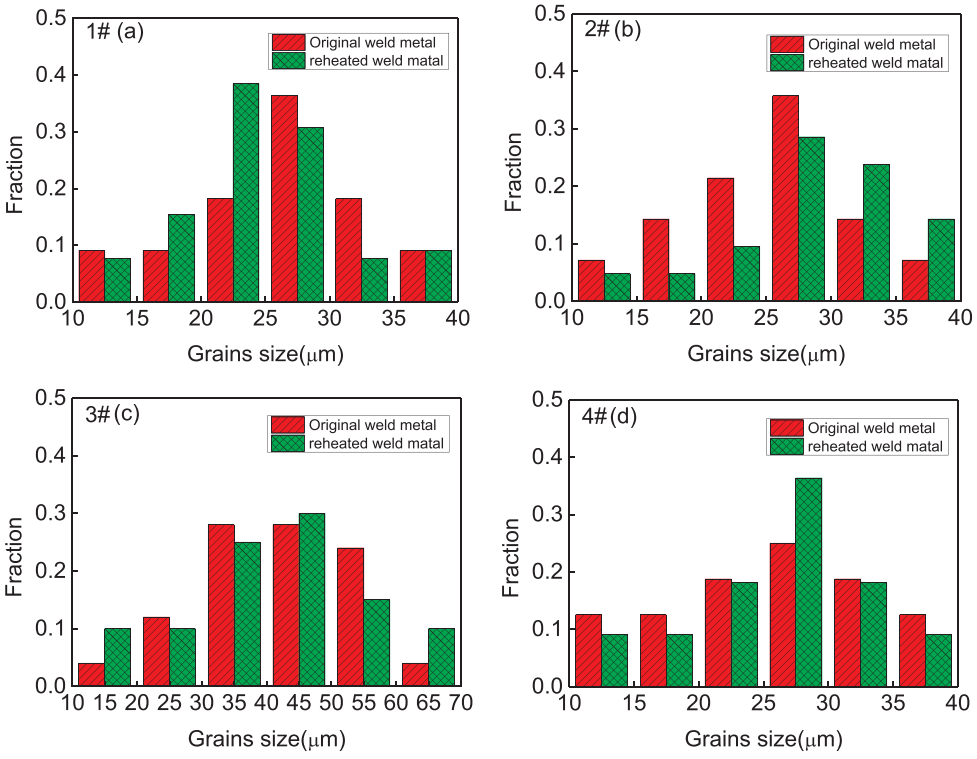

Fig. 7. Grain size of four weld metals.

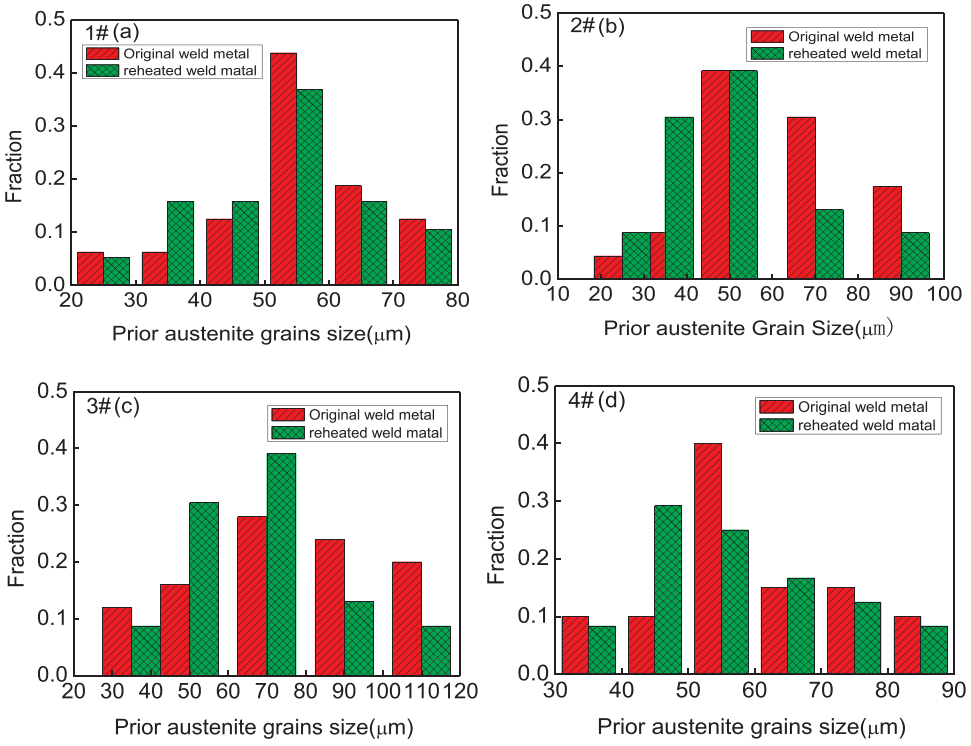

Fig. 8. Prior austenite grain size of four weld metals.

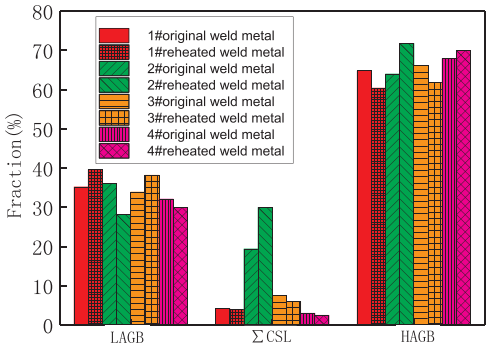

Fig. 9. Distribution of grain boundary of four weld metals.

and various Cu contents, with the increase of Cu content from 0.045% to 0.188%, the width of dimples seems to increase.

At the transition temperature zones and lower shelf zones, the fracture starts with a fibrous crack and then transfer to cleavage fracture modes. Before the initiation of cleavage cracking a preceding fibrous crack with length (SCL) and a narrow stretch (crack blunted) zone SZW are found as shown in Fig. 17. For the specimens with various Charpy toughness, the length of SCL and SZW are different, and thus the initiation of the cleavage fracture begins early or later. Based on above observations on fracture surfaces, it can be seen that the observed stretch zone width (SZW) and the fibrous crack length (SCL) are consistent with that expected by the load-displacement curves in Fig. 2. Results of measurements are drawn in Fig. 18. It can be seen that the total lengths of SZW plus SCL increase with the increase of the testing temperature for all specimens with various weld metals. The energy absorbed in Charpy tests increase with the increase of the SZW plus SCL as depicted in Fig. 18(c). Fig. 18(e) shows the variation of the crack initiation energy with the increase of the stretch zone width (SZW). The increasing rate of the crack initiation energy is 0.109 J per unit SZW. Fig. 18(f) shows the variation of the crack propagation energy with the increase of the fibrous crack length (SCL). The increasing rate of the crack propagation energy is 0.0179 J per unit SCL. Although the rate of energy rise for unit SZW is much higher than that for unit SCL, however by comparing the Fig. 18 the much longer SCL offsets this superiority and contributes the dominant absorbed energy. Because in Fig. 18, all experimental points are measured at various temperatures for specimens with various weld metals, the near linear relationship between the impact energy and the SCL means the absorbed energy for unit length extension of the fibrous crack (unit SCL) is the same for all specimens tested at various temperatures and with various weld metals. As a result, the total crack propagation energy measured in the transition temperature region is mainly determined by the length of the fibrous crack extended. For all specimens, the maximum of the stretch zone width SZW is limited to about 30–300 μm and the corresponding crack initiation energy is about 3–40 J. When test is carried out at the transition temperature, the fibrous crack is initiated and propagated and the crack propagation energy dominates the total impact energy. In this case, the total impact energy is decided by the extended length of the fibrous crack, which in turn is determined by the moment when the cleavage fracture is triggered. When the test is carried out at the lower shelf stage, SCL + SZW is very smaller, thus the fracture starts directly from cleavage, in this case the cleavage distance x_f determines the value of the Charpy toughness. So the initiation origins of cleavage fracture are important. Fig. 19 presents the initiation origins of cleavage fracture at the lower shelf stage and transition stage. The fracture of four weld metals is initiated from the oxidation inclusions at −196 ℃. The initiation origins of 1# and 2# weld metals are the oxidation inclusion including elements Fe、Ti、Mn、Si、S. However, the initiation origins of 3# and 4# weld metals are also oxidation inclusion however including elements Fe, Mn, Si, S, Ni, Al. And it was found that the contents of elements Si and Al increase in 3# and 4# specimens. Chemical compositions on Charpy fracture surfaces are listed in Table 7.

3.8. Results of FEM calculation

Using the hardening model with dynamic yield strength σ_{yd} , the curves of distributions of stress, strain, and stress triaxiality ahead of the notch(Charpy V specimens) at −196 ℃ were calculated by ABAQUS code and are displayed in Fig. 20. Putting the fracture distance

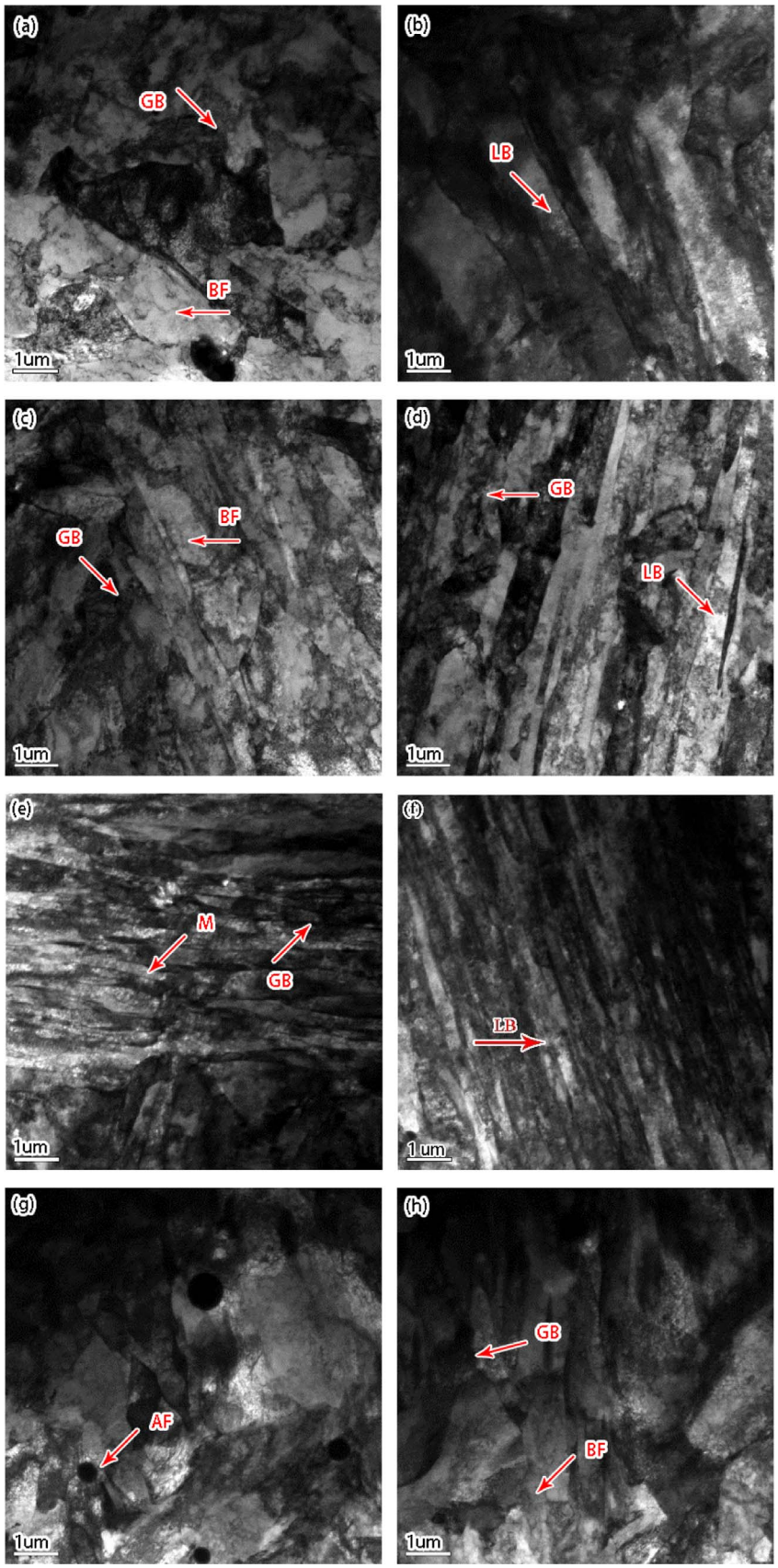

Fig. 10. TEM images of four weld metals (a) (b) 1#, (c) (d) 2#, (e) (f) 3#, (g) (h) 4#.

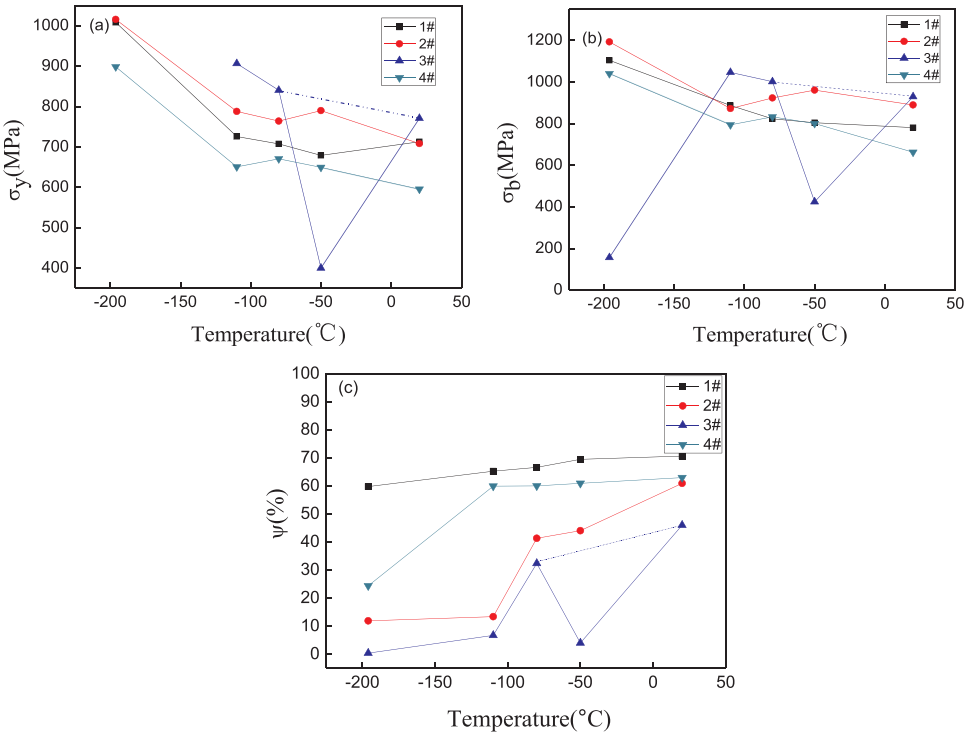

Fig. 11. Parameters of (a) yield strength, (b) ultimate tensile strength, (c) the reduction rate of fracture area with various testing temperatures.

Fig. 12. Fracture mode of 1# tensile specimen.

X_f on the abscissa and drawing a vertical line from it, the corresponding ordinate values on the curves of stress, strain, and stress triaxiality are taken as the local cleavage fracture stress σ_f, the fracture strain ε_{pc}, and the critical stress triaxiality Tc. The measured value of σ_f are 1628 MPa, 1576 MPa, 1245 MPa, 1735 MPa respectively.

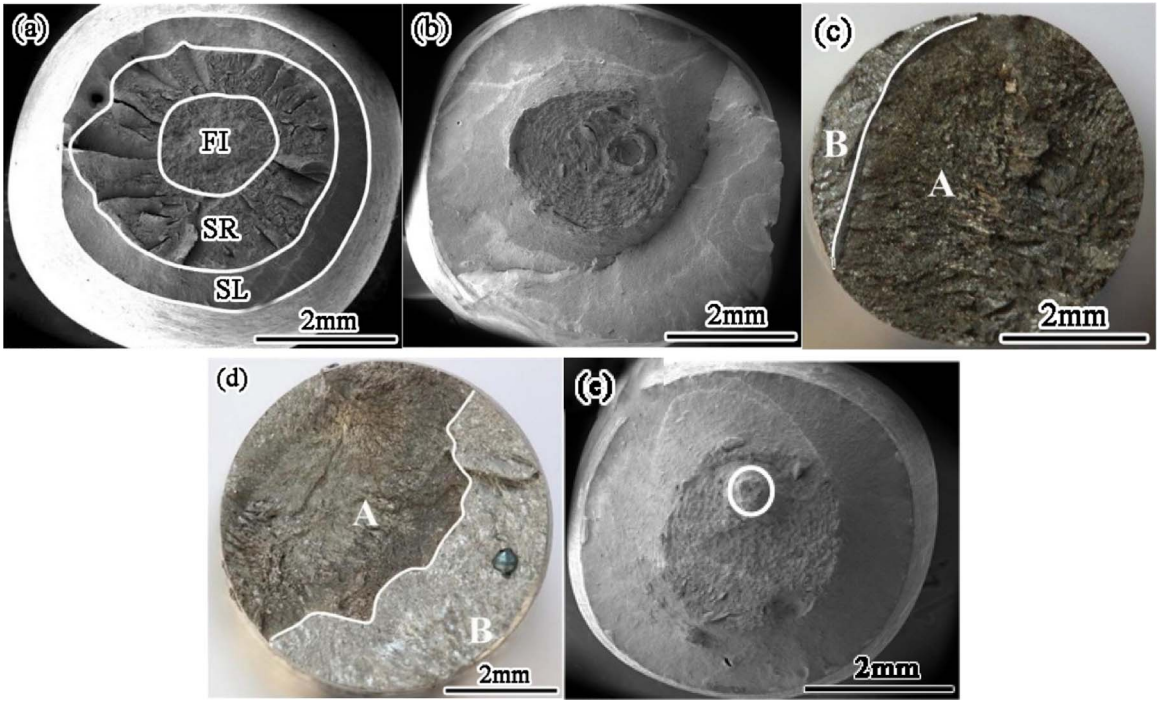

Fig. 13. Macro-fracture surfaces of four tensile specimens at various testing temperature (a) for 1# specimen at −50 ℃, (b) for 2# specimen at −50 ℃, (c) for 3# specimen at −50 ℃, (d) for 3# specimen at −196 ℃ (e) for 4# specimen at −50 ℃.

Table 6
Chemical compositions on tensile fracture surfaces of 3# tensile specimen in Fig. 10 at (−50 °C) (at%).

Region	Point	Fe	O	Si	Mn	Ni	Cr	Mo	Zr
A	1	86.3	5.1	5.1	1.6	1.6	0.3	0.0	0.0
	2	87.2	5.1	3.9	1.6	1.7	0.3	0.2	0.0
	3	93.8	2.4	1.0	1.7	0.8	0.3	0.0	0.0
	4	89.2	2.9	4.0	1.7	1.7	0.3	0.3	0.0
B	1	95.4	0.0	1.2	1.8	1.2	0.3	0.1	0.0
	2	96.1	0.0	1.1	1.6	1.0	0.3	0.0	0.0
	3	94.2	0.0	2.4	1.6	1.4	0.3	0.0	0.0
	4	92.6	1.4	2.7	1.5	1.5	0.3	0.0	0.0

4. Discussions

4.1. The effect of Silicon and Copper on the microstructure of weld metals

For all weld metals in this study from Fig. 5 and Fig. 10, ferrite and bainite mainly dominated the microstructures of weld metals. For the original weld metals, with the increase of Si content, the content of GB increases, the content of LB decreases, and its HV hardness also increased, which is consistent with the results of Ghasmi et al. [17]. Ref. [17] indicated that Si can significantly increase the relative content of granular bainite in low carbon alloy steel. In our experimental results, when the Si content increased to 2%, amounts of martensite appeared, which is also identified by Laird et al. [18]. In Ref. [18], the authors indicated Si reduces the C solubility in austenite and raises the martensite start (M_S) temperature and thus the hardness increases. Table 5 show the size histograms of the prior austenite grains and sub-grains of the four weld metals. The increase of Si content results in the increased size of the prior austenite grains. However, the increase of Si content doesn't obviously change the high angle grain boundary density as shown in Fig. 9. Ref. [19] indicated that the optimization of grain boundary character distribution increased the resistance to fracture crack initiation and extension, then increased the strength, plasticity and toughness of stainless steel. In Ref. [19], the increase of Σ from 54.55% to 70.74% resulted in the increase of about 100 MPa of yield strength, about 200 MPa of the tensile strength, about 10% increase of the plastic deformation capacity and 33% increase of the impact toughness. However, in Fig. 9, it was found that the fraction of the Σ has little influences on the toughness of weld metal.

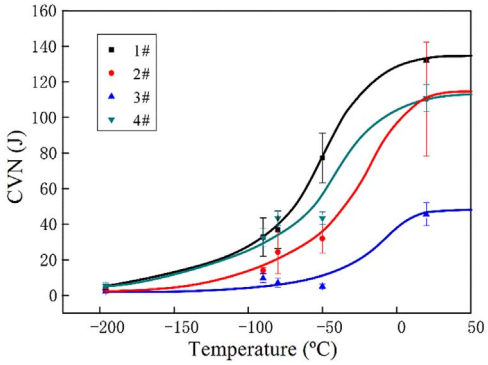

Fig. 15. Relationships between charpy toughness and testing temperature.

The Cu in the austenite can significantly reduce the bainite transition temperature in the austenite cooling processes. Fig. 5 indicated the increase of Cu content leads to the decrease of the lath bainite and overall microhardness, increase of prior austenite grains and the ferrite phase content. However, the increase of Cu content has not obviously affected the high-angle grain boundary.

4.2. The effect of Silicon and Copper on the tensile properties of weld metals

From Fig. 11, at the same testing temperature, with the increase of Si content, the ultimate tensile strength (σ_b), yield strength (σ_y) increase, the fracture area reduction rate decreases, which are related to the change of the microstructure in Fig. 5, ie. the microstructure is changed from the ferrite to granular bainite. With the increasing of Cu, the σ_b and σ_y, the fracture area reduction rate decrease, which is attributed to the coarser of prior austenite and grain size, decrease of LB.

Especially, in 3# weld metal, there has been a typical hydrogen cracking. Hydrogen-induced cracks, also known as cold cracks, mainly appear in the heat-affected zone of high carbon steel and medium carbon steel, low alloy high strength steel, etc., and it is related to the hardening tendency of weld metal. The path of Hydrogen-induced crack fracture sometimes in the form of trans-granular, sometimes in the form of crystals, which is determined by the microstructure of the material, the content of hydrogen and the stress state of the material. There are three reasons for hydrogen cracking: (1) the higher hydrogen content is

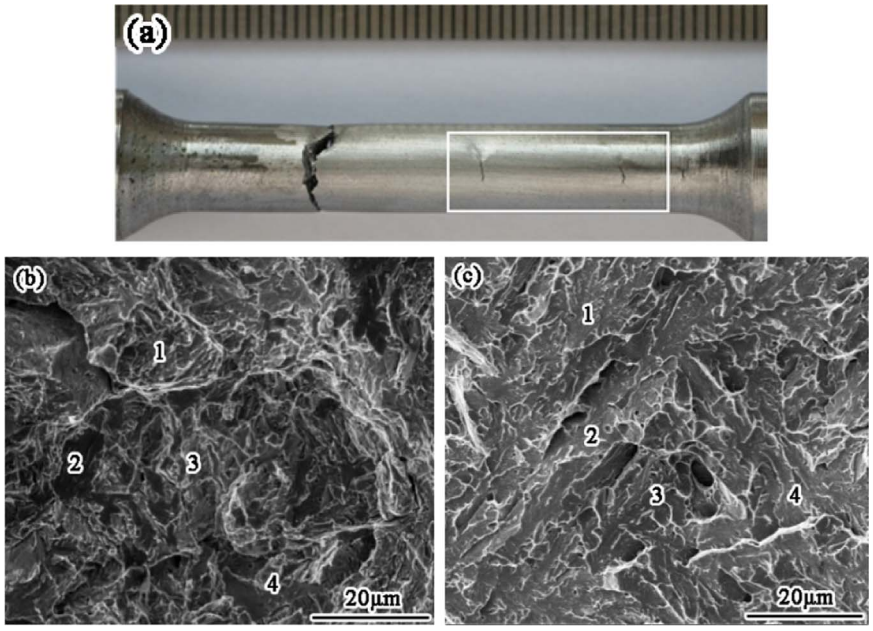

Fig. 14. Tensile fracture surface of 3# specimen at −50 °C(a) macro-fracture mode, (b) region A, (c) region B.

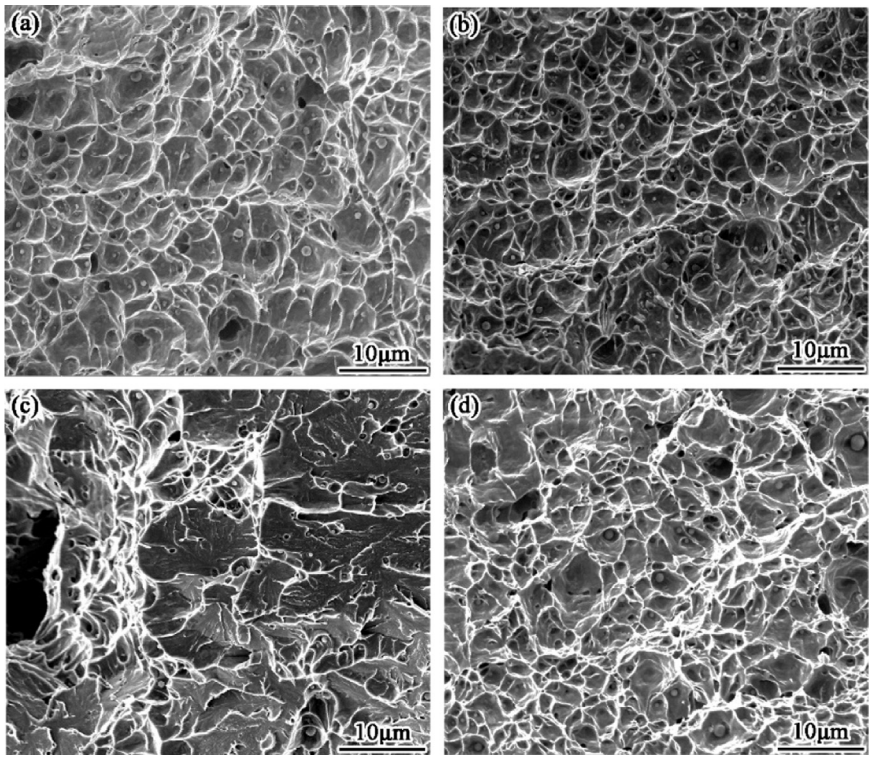

Fig. 16. Impact fracture surface at room temperature. (a)1#, (b) 2#, (c)3#, (d)4#.

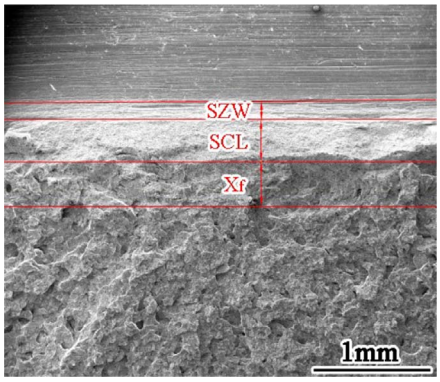

Fig. 17. Macro-fracture surfaces of the lower testing temperature.

an important factor in the cold cracking of high strength steel welded joints. Base metal, water, oil, rust on the wire and environmental humidity are all sources of hydrogen enrichment in the weld. Before welding, the surface of the welding material is not strictly cleaned, it is likely to cause hydrogen enrichment in the weld metal. (2), There are some martensite in the weld metal. The energy consumed by the fracture of martensite phase is smaller because martensite is more brittle. Crack is easy to form and expand when the microstructure contains martensite. The microstructure of the material is one of the important factors to determine the performance of the material, and the hydrogen induced cracking is the most sensitive to the un-tempered martensite. (3) The higher stress in the local area of the weld metal results in stress concentration, finally induces the cracking. Hydrogen-induced cracking is the result by the combined effect of the above three factors. During the cooling process, the heat affected zone undergoes phase transformation before the welding, so the hydrogen element diffuses from the heat affected zone to the weld metal which resulted in the enrichment of hydrogen in the weld.

4.3. The effect of Silicon and Copper on the Charpy toughness of weld metals

With the increase of Si and Cu content, DBTT increases, it means that the impact toughness was decreased. With the increase of Si content, the coarsening of the microstructure, the increasing of GB, decreasing of LB and appearing of lots of M are the reasons for the decrease of the impact toughness. So the 3 # weld metal has the lowest impact toughness.

From Fig. 19(a), (b), (c) and (d), fully cleavage fracture mode dominates the fracture modes of all weld metals at −196 ℃, which is essentially different from that of the upper shelf region (showed in Fig. 16). The critical event for cleavage fracture in a notched specimen is the propagation of a ferrite grain (or a bainite packet)-sized crack. The global fracture occurs once the cleavage microcracking is triggered, which is controlled by criteria

$$\sigma_{yy} \geq \sigma_f \tag{2}$$

Where σ_{yy} is the normal stress ahead of the notch root which is intensified from σ_y through the formula $\sigma_{yy} = Q\sigma_y$. In C-Mn steels, the grain size (the packet size for the bainitic steel) puts a decisive effect on the global fracture toughness by determining both the yield stress σ_y and the local fracture stress σ_f and determining the size of critical event. The finer the grain sizes (or packet size for the bainite steel), the higher the critical stress intensification factor $Qc = \sigma_{yy}/\sigma_y = \sigma_f/\sigma_y$ is needed and the higher is the toughness. Correspondingly, the measured values of σ_f are 1628, 1576, 1245, and 1735 MPa and the values of critical values of the stress intensification Qc are 1.6, 1.46, 1.36, and 1.68. These results indicated that with the increasing of Si content, the grain sizes increase, which decreases σ_f and Qc. The measured σ_f and the area of the cleavage facets surrounding the crack initiation sites support the calculated values of the effective surface energy γ fluctuating in a reasonable range, which are 268, 321, 295 and 217 respectively.

As displayed in Fig. 15, DBTT for weld metals 1, 2, 3 and 4# are −60 ℃, −41 ℃, −18 ℃, −56 ℃, respectively. For weld metal 1, 2 and 3#, the rise of the DBTT means the decrease in toughness at a certain temperature in the transition shelf region, which should be attributed to

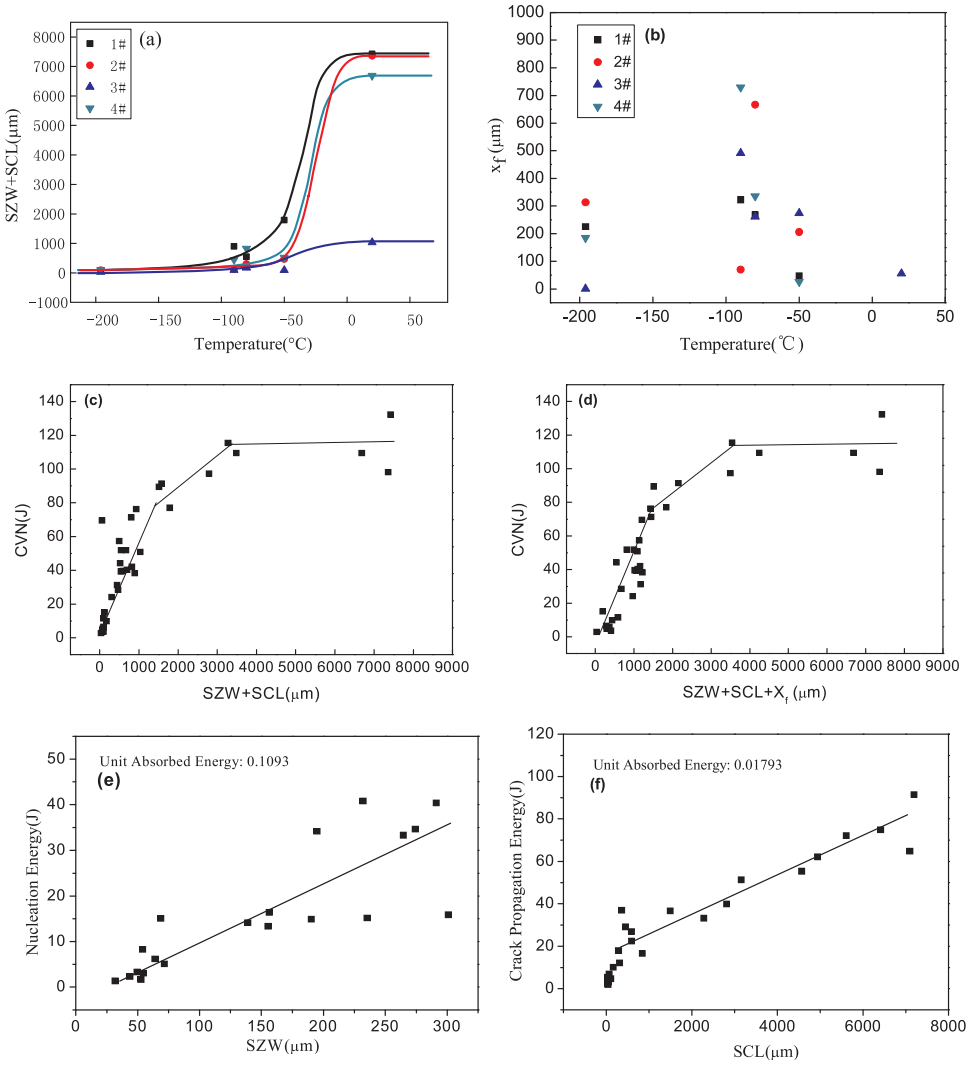

Fig. 18. Relationships between impact energy with SZW, SCL and X_f. (a)Stretch zone width (SZW) plus fibrous crack length (SCL) measured at various temperatures in specimens with various weld metals, (b)X_f at various temperatures in specimens with various weld metals, (c) Plots of the impact energy with stretch zone width (SZW) plus fibrous crack length (SCL) measured at various temperatures in specimens with various weld metals, (d) Plots of the impact energy with SZW + SCL + X_f measured at various temperatures in specimens with various weld metal, (e) Variation of the crack initiation energy with the increase of the stretch zone width (SZW) measured at various temperatures in specimens with various weld metal. (f) Variation of the crack propagation energy with the increase of the fibrous crack length (SCL).

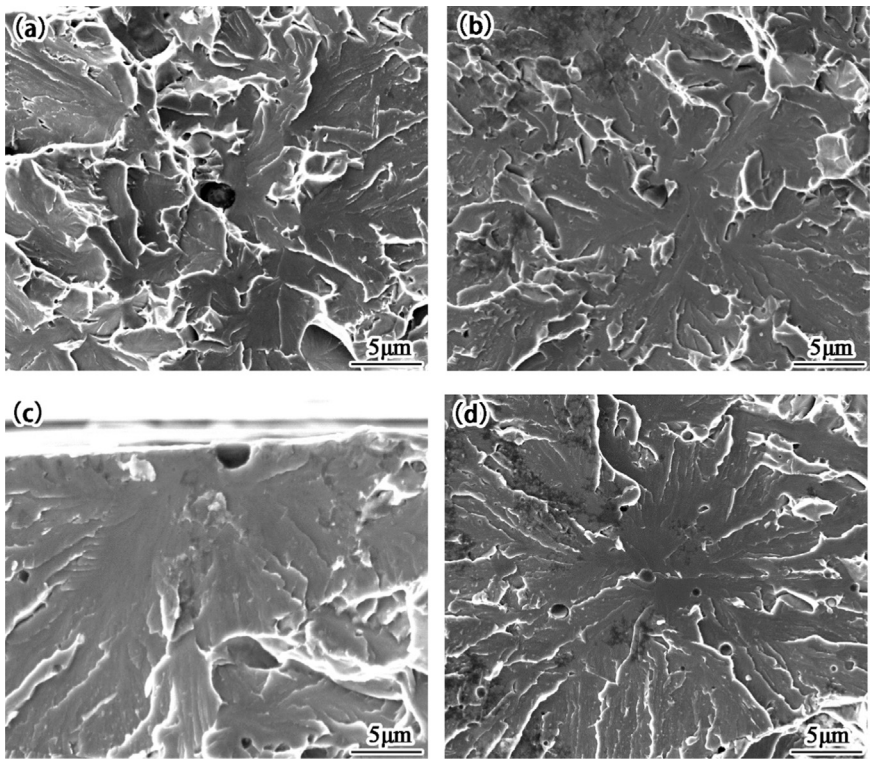

Fig. 19. Fracture surfaces of Charpy V specimens with various weld metal fractured at −196 °C. (a)1#, (b)2#, (c)3#, (d)4#.

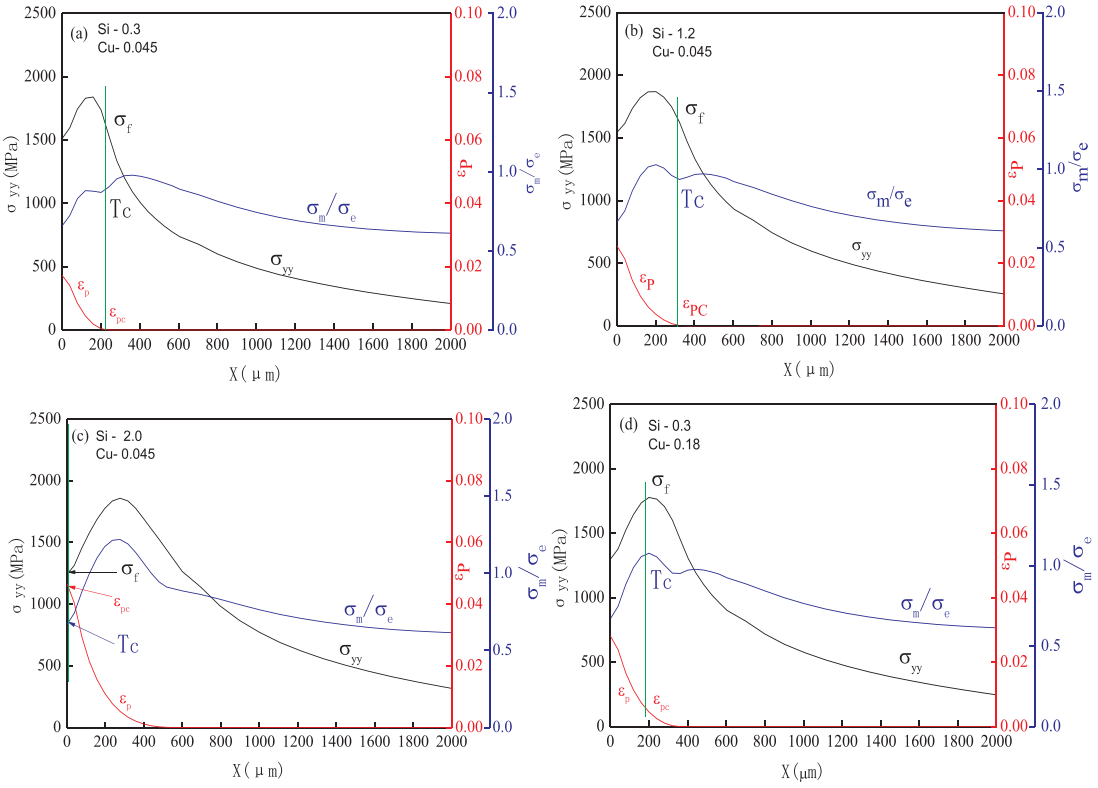

Fig. 20. Distribution curves of stress, strain, and stress triaxiality ahead of the notch at 77 k (−196 °C).

Table 7
Chemical compositions on Charpy fracture surfaces (at%).

	Fe	O	Si	Mn	Ti	Ni	Al	Cr	S
1#(−196 °C)	10.5	66.3	3.2	6.8	12.6	0.1		0.1	0.5
2#(−196 °C)	19.8	53.8	3.8	3.2	11.7	0.2	7.2	0.1	0.2
3#(−196 °C)	83.1	8.9	4.8	1.6		1.3	0	0.2	0
4#(−196 °C)	90.1	4.4	1.7	2.1		1.5	0	0.3	0

the increases of the maximum grain size and change of the microstucture due to the increases of the Si content. For weld metal 1 and 4#, the slight increase of the DBTT means the decrease in toughness at a certain temperature in the transition shelf region, which should be attributed to the increases of the maximum grain size (larger cleavage facet size) due to the increases of the Cu content. This is the micromechanism of change of impact toughness in the lower shelf temperature region with the change of Si and Cu.

5. Conclusions

In the present study, the four weld metals with different Silicon and Copper contents are investigated in details.

1. Si addition decreases the impact toughness of the weld metal and also changes its microstructure. The prior austenite grain size is increased by with the Si addition, and the microstructure changes from BF + GB to GB + LB + M, which finally induced the deterioration in toughness. When the Si content is increased to 2.0 wt%, The welded structure is very uneven and a typical hydrogen cracking presents.
2. Cu addition decreases the impact toughness of the weld metal a little, and also changes its microstructure. The prior austenite grain size is increased by the Cu addition, the content of granular bainite in the weld metal decreases, but the ferrite content increases, which induced the slight decrease of the toughness.
3. DBTT increases with the increase of Si content. DBTT increases with the increase of Cu content.
4. The fraction of ΣCSL and HAGB have little influence on the toughness of the weld metal.
5. With the increase of Si content, σ_f decreases from 1628 to 1576 and 1245 MPa. The decrease of σ_f makes the cleavage fracture easier and decreases the toughness in the lower shelf region. It also makes the termination of the extension of the fibrous crack early and cuts down its length, thus decreases the toughness in the transition temperature region.

Acknowledgements

This work was financially supported by National Nature Science Foundation of China (Nos. 51761027, 51675255), the Program of Innovation Groups of Basic Research of Gansu Province (17JR5RA107) and The Foundation of Collaborative Innovation Teams in College of Gansu Province (2017C-07). Thanks to Hobart Brother companies in the United States on the experiment of support and discussion of experimental results, and their comments and suggestions of the editors and reviewers.

References

[1] Satish Kumar Sharma, Sachin Maheshwari, A review on welding of high strength oil and gas pipeline steels, J. Nat. Gas. Sci. Eng. 38 (2017) 203–217.
[2] C.J. Trench, J.F. Kiefner, Oil Pipeline Characteristics and Risk Factors: Illustrations from the Decade of Construction, 2001.
[3] Z. Zhu, J. Han, H. Li, Effect of alloy design on improving toughness for X70 steel during welding, JMADE 88 (2015) 1326–1333.
[4] F.S. Jaberi, A.H. Kokabi, Influence of nickel and manganese on micro-structure and mechanical properties of shielded metal arc-welded API-X80 steel, J. Mat. Eng. Perform. 21 (2012) 1447–1454.
[5] H.K. Sung, S.S. Sohn, Y.S. Sang, K.S. Oh, S. Lee, Effects of oxides on tensile and charpy impact properties and fracture toughness in heat affected zones of oxide-containing API X80 linepipe steels, Metall. Mater. Trans. A. 45 (2014) 3036–3050.
[6] H.K. Sung, S.Y. Shin, W. Cha, K. Oh, S. Lee, N.J. Kim, Effects of acicular ferrite on

charpy impact properties in heat affected zones of oxide-containing API X80 line-pipe steels, Mater. Sci. Eng. A528 (2011) 3350–3357.
[7] M.H. Shi, X.G. Yuan, H.J. Huang, S. Zhang, Effect of zr addition on the micro-structure and toughness of coarse-grained heat-affected zone with high-heat input welding thermal cycle in low-carbon steel, J. Mater. Eng. Perform. 26 (2017) 1–9.
[8] A.M. Guo, S.R. Li, J. Guo, P.H. Li, Q.F. Ding, K.M. Wu, X.L. He, Effect of zir-conium addition on the impact toughness of the heat affected zone in a high strength low alloy pipeline steel, Mater. Charact. 59 (2008) 134–139.
[9] I.I. Frantov, A.A. Velichko, A.N. Bortsov, I.Y. Utkin, Weldability of niobium-containing high-strength steel for pipelines, Weld. J. 93 (2014) 23–29.
[10] X. Chen, G. Qiao, X. Han, X. Wang, F. Xiao, B. Liao, Effects of Mo, Cr and Nb on micro-structure and mechanical properties of heat affected zone for Nb-bearing X80 pipeline steels, Mater. Des. 53 (2014) 888–901.
[11] J.E. Ramirez, Characterization of high-strength steel weld metals: chemical composition, micro-structure, and nonmetallic inclusions, Weld. J. 87 (2008) 65–75.
[12] K. Sirin, S.Y. Sirin, E. Kaluc, Influence of the chemical composition of weld electrode on the mechanical properties of submerged arc welded pipe, Int. J. Adv. Manuf. Technol. 87 (2016) 1941–1950.
[13] W.M. Garrison, The effect of silicon and nickel additions on the sulfide spacing and fracture toughness of a 0.4 carbon low alloy steel, Metall. Trans. A. 17A (1986) 670–671.
[14] G. Laird, G.L. Powell, Solidification and solid-state transformation mechanisms in Si alloyed high-chromium white cast irons, Metall. Trans. A. 24 (1993) 981–988.
[15] Sang Yong Shin, Seung Youb Han, Byoungchul Hwang, Chang Gil Lee, Sunghak Lee, Effects of Cu and B addition on microstructure and mechanical properties of high-strength bainitic steels, Mater. Sci. Eng. A. 517 (2009) 213–214.
[16] J.H. Chen, R. Cao, Micromechanism of Cleavage Fracture of Metals, Elsevier, USA, 2014.
[17] S.S. Ghasmi, K.K. Banad, D.P. Dunne, Age hardeningin a Cu-bearing high strength low alloy steel, ISIJ Int. 36 (1996) 61–67.
[18] G. Laird, R. Gundlach, K. Rohrig, Abrasion-resistant Cast Iron Handbook, USA, 2000.
[19] X. Xu, S. Yang, The Effect of Grain Boundary Design and Control on Mechanical Behavior of 304 Austenitic Stainless Steel, Nanjing University of Science and Technology, 2013 (Master Dissertation).